Environ Earth Sci (2014) 72:3383–3399
DOI 10.1007/s12665-014-3244-3

ORIGINAL ARTICLE

Modelling of hydraulic fracturing process by coupled discrete element and fluid dynamic methods

Sousani Marina · Eshiet Kenneth Imo-Imo · Ingham Derek · Pourkashanian Mohamed · Sheng Yong

Received: 31 July 2013 / Accepted: 28 March 2014 / Published online: 17 April 2014

Abstract A three-dimensional model is presented and used to reproduce the laboratory hydraulic fracturing test performed on a thick-walled hollow cylinder limestone sample. This work aims to investigate the implications of the fluid flow on the behaviour of the micro-structure of the rock sample, including the material strength, its elastic constants and the initialisation and propagation of fractures. The replication of the laboratory test conditions has been performed based on the coupled Discrete Element Method (DEM) and Computational Fluid Dynamics scheme. The numerical results are in good agreement with the experimental data, both qualitatively and quantitatively. The developed model closely validates the overall behaviour of the laboratory sample, providing a realistic overview of the cracking propagation towards total collapse as well as complying with Lame's theory for thick-walled cylinders. This research aims to provide some insight into designing an accurate DEM model of a fracturing rock that can be used to predict its geo-mechanical behaviour during Enhanced Oil Recovery applications.

Keywords Hydraulic fracturing · Hollow cylinder · Porous flow · Fluid injection · 3D modelling

S. Marina · I. Derek · P. Mohamed
Energy Technology and Innovation Initiative (ETII), University of Leeds, Leeds LS2 9JT, UK

S. Marina · E. K. Imo-Imo · S. Yong (✉)
School of Civil Engineering, University of Leeds, Leeds LS2 9JT, UK
e-mail: y.sheng@leeds.ac.uk

Introduction

There is a clear relationship between the increase of CO_2 and human activities (Mikkelsen et al. 2010; IPCC 2007a, b). Industrialisation contributes greatly to the rise of greenhouse gas emissions and carbon capture, and storage technology plays an essential role as part of the mitigation plan for the reduction of CO_2 levels in the atmosphere. Storage of CO_2 within deep geological formations is a very promising option and the technology has been used successfully for years in major projects, such as in flow metering in the USA and in the oil and gas industry (Jin et al. 2012). Specifically in the USA, the transition from conventional oil reservoir drilling to hydraulic fracturing of gas reservoirs has been rapidly developing over the last decade. Being part of the well-known technology used for oil extraction, it was considered a minor technological step forward thus lacking the development of necessary regulations for environmental safety and sustainability of the hydraulic fracturing technology. The major effects are the possible contamination of shallow groundwater layers by the migration of the toxic components of the fracturing fluid and flowback fluids as well as the leakage of methane, which acts as a greenhouse gas, into the atmosphere.

Flowback fluid mainly consists of formation fluid and hydraulic fracturing fluid thus there is a potential risk of contamination of freshwater resources if flowback fluid is allowed to flow uninhibited. Fracturing fluids contain hazardous substances; the exposure of these chemicals and risk to groundwater reserves is linked to factors including underground fluxes and the concentration of hazardous substances in fracturing fluids (Gordalla et al. 2013). Already an ecotoxicological assessment of undiluted fracturing fluids indicates a hazardous effect on aquatic life (Riedl et al. 2013). Generally, flowback fluids contain a

high ratio of formation fluid to fracturing fluid. The potency of flowback fluid depends on the mix ratio of the formation fluid and fracturing fluid and although a high proportion of fracturing fluid may be retained in the formation (Olsson et al. 2013), there is high tendency for flowback to take place as a result of imposed fracturing operations. Some methods have been proposed by Olsson et al. (2013) for categorising and treating flowback fluids.

In comparison to the impact of fracturing fluids, freshwater reserves are more prone to be polluted by flowback water (Gordalla et al. 2013). Risk assessments carried out by Lange et al. (2013) identifies fault zones as preferential pathways that facilitate the movement of fracturing fluids in unconventional gas reservoirs, thereby increasing the possibility of groundwater contamination. However, similar assessments conducted by Kissinger et al. (2013) discuss the potential and contributions of other flow paths (e.g. poorly sealed wells).

Public concern has forced countries to seek expert opinion with the example of Germany and the ExxonMobil initiative. The latter has formed a multidisciplinary working group to identify the possible environmental risks for the Lower Saxony Basin. Their role is to evaluate the available technology (drilling and technical procedures) and develop a suitable strategy for safe hydraulic fracturing operations. More specifically the "*Information and Dialogue process on hydraulic fracturing*", as part of the strategy, focuses on the overall assessment approach, the characterisation of the hydrogeological system, the potential leakage flow paths and circumstances under which leakage may occur (chemical underground interactions), the development of suitable models, and finally the discussion of the simulated results (Lange et al. 2013; Kissinger et al. 2013). Apart from risks due to subsurface activities, there are above-surface hazards linked to the transport and storage of fracturing fluid additives, and infrastructure and landscape planning.

Groundwater is Germany's basic resource for drinking water; thus, the toxicological investigation of the ingredients of the fracturing fluid as well as the influence of the flowback and potential hazards has been a priority (Olsson et al. 2013). However, the lack of available data of the pollutants and their chemical composition in flowback is a barrier for the German and European fracking operations. Recent studies are focusing on the ecotoxicological risks of the used chemicals to fill the knowledge gap and recommend the critical areas for future investigation. An example is the work by Riedl et al. (2013) where flowback volumes and characteristics are estimated, groups of pollutants are identified and appropriate treatment technologies are recommended.

Enhanced Oil Recovery (EOR) and/or Enhanced Gas Recovery (EGR) is regarded as one of the effective schemes for a low-carbon energy future, since CO_2 injection and oil/gas extraction from hydrocarbon reservoirs can be done concurrently (Blunt et al. 1993; Parker et al. 2009; Jin et al. 2012). However, the whole process requires a considerable pressure to introduce liquefied CO_2 underground, thus causing redistribution of the in situ effective stresses within the reservoir. Although in this process the fracturing of the reservoir is desirable, such stress changes may induce irreversible effects to the rock strata, thus causing possible reactivation of the existing faults that may lead to possible leakage of CO_2 (IEAGHG 2011b; Wilkins and Naruk 2007) and potential hazards such as contamination of shallow groundwater aquifers and/or methane emissions (Kissinger et al. 2013). Therefore, valid estimates of the mechanical behaviour of the rock material under intense injection conditions are crucial to the efficient planning and operation of hydrocarbon reservoirs.

Extended research has been performed to investigate the wellbore instability for hard and low porosity sedimentary rocks (Zhang et al. 1999; Jaeger et al. 2009), as well as changes of rock permeability with in situ stresses (Holt 1990; Bachu and Bennion 2008; Bouteca and Vincke 2000; Bruno 1994; Bryant et al. 1993; Ferfera et al. 1997). Furthermore mathematical solutions and experimental models have been developed to look into critical mechanical parameters such as the stress envelope and crack network or the way that these are influenced by the induced stress regime (Aminuddin 2011; Ziqiong 1989; Eslami and Hoxha 2010; Hanson et al. 1980). However, while there are some studies dealing with modelling and simulation of rocks at the micro-scale (Gil et al. 2005; Tomiczek 2003; Akram and Sharrock 2009; Potyondy and Cundall 2004; Li and Holt 2001; Funatsu et al. 2007; Eshiet et al. 2013; Martinez 2012) the complex interplay between the micro-properties of a virtual sample and their corresponding effect on the material's behaviour during the calibration procedure provides a general guidance at best. Part of this study deals with the adopted methods and even though the description of the way values of the calibration procedure is given in summary, it may serve as future reference for other researchers.

The DEM (Discrete Element Method) approach is utilised to simulate the behaviour of materials such as sandstone and limestone, including discontinuities such as joints, fractures and/or faults and the fluid–solid interactions among them (Potyondy and Cundall 2004; Walton 1987; Chang 1987). The Lattice-Boltzmann method of computing fluid flow solves the discretised form of the Boltzmann equation which is based on the Navier–Stokes equation (Chen and Doolen 1998). Other methods of computing fluid flow include Direct Numerical Simulation (DNS) (Dong 2007; Moin and Mahesh 1998) and Computational Fluid Dynamics (CFD). The need to provide linkages between co-existing fluid and solid

phases necessitates a coupling of these techniques with the modelling of solid mechanics such as DEM. The Lattice-Boltzmann and DEM coupling is illustrated in (Boutt et al. 2007), while approaches that incorporate CFD with DEM have been presented (Xu and Yu 1997; Tsuji et al. 1993). Most of these coupling schemes are applied to granular or uncohesive materials and in cases where the domain is dominated by fluid phases. Therefore, phenomena such as the deformation of the solid material and fracturing are not captured due to either the limitation of the coupling technique or the delineation of study. This study also deals with the fluid–solid interaction incorporating the DEM technique in PFC3D (Particle Flow Code 3D) (Itasca-Consulting-Group 2008a) and demonstrates an extension of its applicability via the modelling of hollow cylinder laboratory tests. Applications of this sort, where direct numerical and experimental comparisons were carried out, are still lacking.

In the PFC3D model, the particles are connected by parallel bonds that replicate the cementation between grains in actual rocks. The macroscopic behaviour of the material is derived from statistical assumption of the interactions between the particles of the assembly used to represent the rock sample. Hence, large particle numbers will provide more accurate results. The simulation time was a key limitation, given the available computer processing power. At the moment, computer packages using DEM to study rock micro-parameters are restricted to about 5×10^5 spherical particles for high-powered desktop computing.

Laboratory experiment

Laboratory fracturing experiments are often used to monitor the deterioration and disintegration of rocks under prescribed and controlled simulated sub-surface reservoir conditions. As part of this experimental investigation, a number of tests were conducted on a series of synthetic and natural rock samples subjected to differing operating and boundary conditions. Artificial samples were created to imitate soft permeable rocks that are low in strength (bonded glass bead materials), while the natural samples consisted of limestone. The early and non-progressive collapse, meaning the sudden disintegration of the synthetic samples during the initial stages of fluid flow, illustrates the combined effects of permeability and strength on the failure mode. This phenomenon is not observed in the limestone samples which are less permeable but have a higher strength. Observed occurrences of pressure build-up, deformation and fracturing during the tests show the role of an operating well and reservoir conditions as well as the physical and mechanical properties of materials on mechanisms that result in collapse failure and the mode of application of injected water inside the sample.

To determine the mechanical behaviour of natural rock under prescribed fluid flow conditions, a set of tests was conducted on a cylindrical limestone sample (37.8 mm diameter and 100 mm height) which was drilled along its axis to create a cylindrical cavity. The test was performed on a specimen with a cylindrical cavity of 21.5 mm sourced from Tadcaster, North Yorkshire, U.K. An initial pressure differential was established between the outside of the specimen and the hollow centre, which was kept at zero pressure. The outer boundary fluid pressure was then gradually increased until failure. The laboratory equipment for the fracturing test included a permeameter combined with a CT scanner and hydraulic hand pumps to drive and regulate the injection fluid at the prescribed pressure through the specimen cavity and around the circumference of the specimen. A set of computers to monitor and control test operations as well as to process the scan images were also included.

Fracture initiation was observed to occur after about 8,000 s and the eventual collapse of the cavity wall occurred at 5,056 Psi (35 MPa) followed by a rapid drop in the circumferential pressure to 29 Psi (Fig. 1). The initial state of the specimen and the progressive fracturing and collapse is illustrated in Fig. 2.

The hydraulic fracturing experiments were performed on a variety of synthetic and natural rock samples and they illustrate a fracturing and failure behaviour that is predominantly influenced by the material mechanical and physical properties, boundary conditions, as well as the mode of application of the injection fluids. It was observed that for soft rocks, i.e. highly permeable, it is generally difficult to reach a significant pressure build-up that will result to inner collapse of the cavity. Furthermore the imminent severe deformation of the material within the outer radius of the sample occurs regardless of the existence

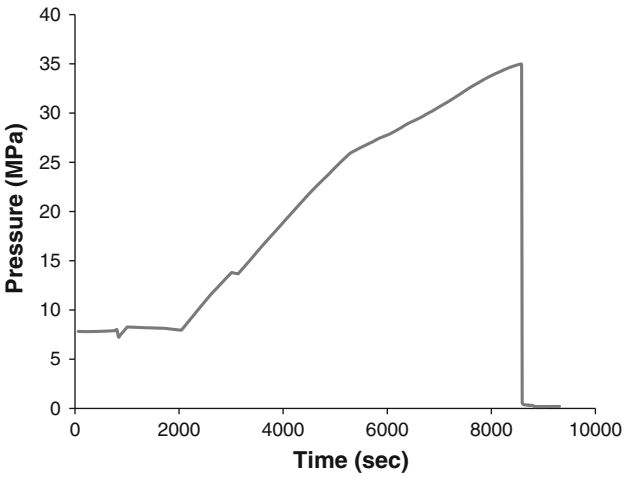

Fig. 1 Fluid pressure differential between the hollow core and the outer surface of the slice, versus time. The maximum fluid pressure differential is 35 MPa

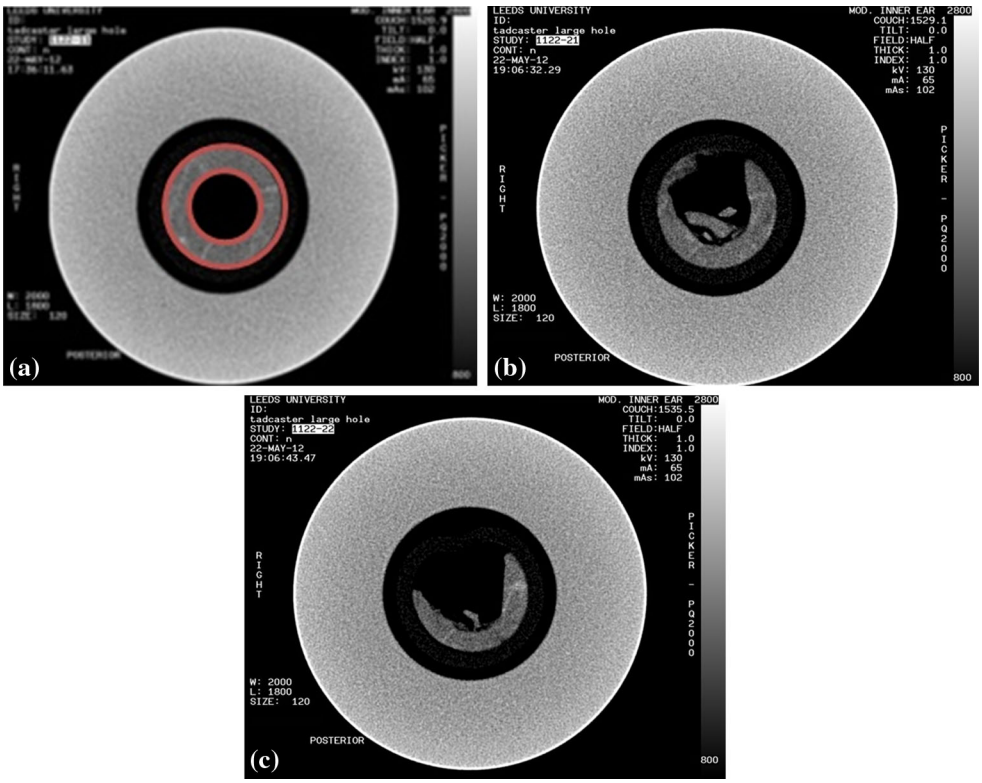

Fig. 2 Scan image of the large cavity limestone specimen inside the test tube **a** in the initial state (*red*), and **b**, **c** in various stages of the collapse of the cavity wall

of a pressure gradient developed between the outer surface and the inner hollow core. When the material strength and stiffness are increased, the maximum allowable build-up fluid pressure also increases. In this case, the integrity of the outer surface of the sample is more likely to be maintained and the process of failure at the cavity is such that there is an initial expansion prior to the collapse of the cavity. More specifically, regarding the limestone sample, the size of the cavity plays a major role which means that larger size cavities appear to be considerably less stable than smaller ones. In any case, sample failure occurs at pressures close to the reported compressive strength of the material. Furthermore, in the cases where externally applied stresses are negligible, initiation and propagation of fractures will always occur perpendicular to the axis of the cavity.

Determination of model parameters

Determination of micro-parameters and sample calibration

This test is built upon the Uniaxial and the Brazilian procedures using the 3D version of PFC. A rectangular model is used to replicate the limestone rock sample tested in the Laboratory of the University of Leeds as previously discussed. The aim of the test is to calibrate the PFC model by matching its maximum Uniaxial Compressive Strength (UCS), tensile strength and elastic properties (Young's modulus E and Poisson's ratio v) with the ones of the laboratory sample obtained from the literature. The calibration process includes a series of simulated Uniaxial and Brazilian tests to investigate and identify the micro-parameters critical to the overall mechanical behaviour of the numerical model.

The DEM method used in this work to represent the solid body of the real rock and its short-term behaviour was based on the characterisation of the virtual specimen in terms of parameters in the micro-scale (Itasca-Consulting-Group 2008c). More specifically, the properties of UCS/tensile strength and elastic constants are macroscopic properties and they cannot be directly described in a DEM model, thus a micro-property process had to be set. This involved the relation between the deformability and strength of the assembly (Young's modulus, angle of friction, Poisson's ratio and strength for particles and bonds) as shown in Table 2, to their equivalent set of macro-responses.

During each Uniaxial test, the specimen was axially compressed by two walls acting as loading platens (Fig. 3), whereas the sample was compressed laterally during the Brazilian test (Fig. 5). The results obtained were monitored

and recorded by three different measurement schemes: specimen-based, wall-based (corrected) and measurement circle-based. The basic difference between the first two schemes is that the specimen-based results are based solely on the observed total stresses and strains applied on the confining walls, whereas in the second case the results are derived from measurements at each ball–wall contact point, where the effect of possible ball–wall overlap has been removed. Finally, the measurement of the circle-based quantities is derived from three measurement circles located in the upper, central and lower portions of the specimen and provides a more uniform averaged response over the entire specimen surface thus was chosen as the best measurement technique for this work.

Uniaxial test with PFC3D

In the simulated Uniaxial test, a rectangular specimen of dimensions 37.8 × 37.8 × 100 mm (Fig. 3) was generated by a standard sample genesis procedure, where the synthetic material consisting of particles and cementation (parallel bonds) is produced in a vessel. The vessel consists of frictionless walls in the *X*, *Y* and *Z* directions forming an isotropic and well-connected virtual assembly. Next, the lateral walls were removed and before enabling the movement of the top and bottom platens, the assembly was cycled to absorb any residual forces that the lateral walls were acting on the sample (Fig. 3-left). The top and bottom walls were used as the loading platens and assigned a constant speed before initiating the test (Fig. 3-right). To represent the real environment of an underground rock sample more realistically, the specimen is initially compressed before the test begins at $P_c = 0.1$ MPa pressure. The loading platens are considered frictionless and with

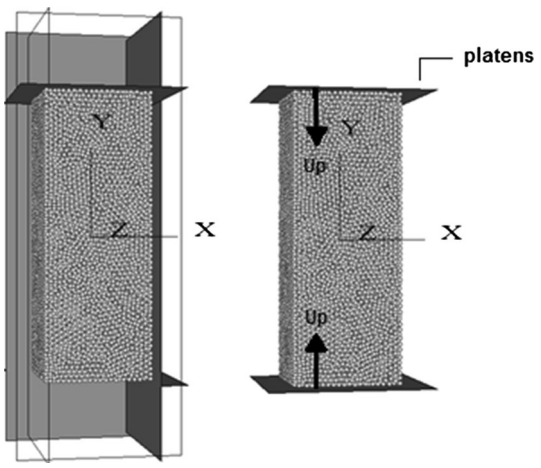

Fig. 3 Schematic of the virtual limestone assembly during the standard genesis procedure (*left*). In the Uniaxial test the sample is loaded by platens moving towards each other at constant speed (*right*)

stiffness much higher than the particles' average one. Furthermore, the loading rate had to be slow enough so that the sample would remain in a pseudo-static state during the entire test. Thus, the velocity was applied gradually reaching its final value in multiple steps so that the developing acceleration will not produce large inertial forces which in turn could cause damage.

Due to lack of appropriate documentation regarding the properties of the laboratory limestone sample, it was considered necessary to obtain the relevant properties from the literature. The UCS, tensile strength and the elastic constants of a real limestone sample from the existing literature are summarised in Table 1. The laboratory limestone sample was a moderately weak one, thus a maximum UCS strength near the lower part of the strength range reported in the literature was sought after for the simulation model.

Initially both the Young's modulus of the particles and bonds were set to 40 GPa, according to the conclusions of Akram and Sharrock (Akram and Sharrock 2009). Depending on their findings, the Young's modulus of the particles is in good agreement with the Young's modulus of the bonds, as long as the stiffness ratio is about 1.0. Even though the referring sample was sandstone, it appears to be appropriate to use this finding in the case of limestone. This is because the two types of rocks are similar and the ratio of the normal and shear stiffnesses was also 1.0. A few trials indicated that the aforementioned micro-parameters should change taking the final value of the Young's modulus of the particles should be $E_C = 30$ GPa, whereas the Young's modulus of the parallel bonds should be $\bar{E}_C = 20$ GPa, lying within the broad range 15–55 GPa (Table 1). Although, there is no guideline concerning the required isotropic stress of the material and the literature does not shed any light regarding a typical value for limestone, the general rule of one-tenth of the target UCS strength of the material was employed. The required isotropic stress is the average of the direct stresses given by:

$$\sigma_o = \frac{\overline{\sigma}_{kk}}{\lambda}, \lambda = 3. \quad (1)$$

Table 1 Typical geo-mechanical properties of limestone, according to the literature (University-of-Stanford; Knill et al. 1970; Hallsworth and Knox 1999)

Limestone parameters	
UCS strength	$q = 30$–250 MPa
Tensile strength	$\sigma_\tau = 5$–25 MPa
Young's modulus	$E = 15$–55 GPa
Poisson's ratio	$v = 0.18$–0.33
Grain size	0.6–2.0 mm
Density	2,500–2,700 kg/cm^3
Porosity	5–30 %

Table 2 PFC micro-parameters used for the Uniaxial simulated test on the limestone model

Micro-parameters that define the sample	Sample height (mm)	100
	Sample diameter (mm)	37.8
	Sample porosity (%)	15
	Initial friction of balls	5.5°
	Gravity (m/s^2)	9.81
Micro-parameters that define the particles	Ball radius (mm)	0.85
	Ball density (kg/m^3)	2,600
	Young's modulus (GPa)	30
	Ball stiffness ratio	1.0
	Required isotropic stress (MPa)	0.4
Micro-parameters that define parallel bonds	Radius multiplier	1.0
	Young's modulus (GPa)	20
	Normal/Shear stiffness ratio (Pa/m)	1.4
	Normal strength (MPa)	30
	Std. deviation of normal strength	30×10^4
	Shear strength (MPa)	30
	Std. deviation of shear strength	30×10^4

It is used to reduce possible unbalanced forces and locked-in stresses (tensile and compressive) during the generation process and provide better internal equilibrium to the assembly. Thus in this case it was set to be one-tenth less than the desired Uniaxial maximum strength. Next, the Poisson ratio was set by defining the ratio of the shear to the normal contact stiffness for both the particles and bonds. A few iterations were carried out to match these micro-properties with the corresponding elastic constants of the material. Once the elastic constants had been matched, the maximum strength of bonds was set near a low desired value within the range 30–250 MPa. A large number of trials had to be executed to finally match and reproduce the relevant behaviour of a limestone rock. Table 2 demonstrates the complete set of input data used for the Uniaxial test.

The test was performed with a velocity of $u_p = 0.005$ m/s and the axial stress (σ_α) was continuously monitored rising to a maximum value and then decreasing as the sample fails. It was terminated when the current value of the sample's axial stress became <0.01 times the previously recorded maximum axial stress value $\left(|\sigma_a| < \alpha \times |\sigma_a|_{\max}\right)$. Using this configuration, the sample showed the expected behaviour in terms of the stress–strain curve, Fig. 4.

Figure 4 clearly indicates that the stress–strain relationship is approximately linear, thus showing that the material is in its elastic regime, until it reaches the point of its ultimate axial strength (46 MPa). Beyond that point, the material enters the plastic deformation regime, indicating

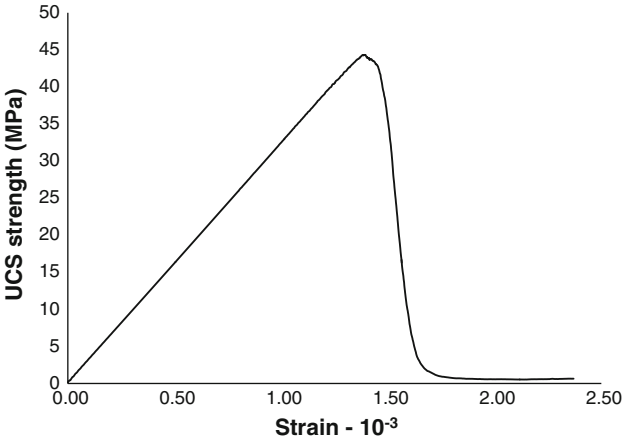

Fig. 4 PFC3D output of the stress versus strain for the limestone assembly used in the simulated Uniaxial test

Table 3 Uniaxial test results of the UCS strength and the elastic constants for the weak simulated limestone model

Uniaxial results (moderately weak sample)	
Elastic constants	$E = 34$ GPa
	$v = 0.21$
UCS strength	$\sigma = 46$ MPa

irreversible damage. Table 3 highlights the results obtained from the Uniaxial test indicating that the material is weak in terms of both the UCS strength and its elastic constants. Further, the Poisson's ratio and the Young's modulus are well within the reported range for limestone formations.

Brazilian test with PFC 3D

In the simulated Brazilian test, the virtual specimen was a cylindrical disc with the same micro-properties obtained from the aforementioned rectangular specimen used in the Uniaxial test (Table 2). A well-connected assembly of uniform size particles was created with genesis procedure and the required stresses were applied so that the sample reached the target isotropic stress. The specimen then was trimmed into a cylindrical disc of 50 mm diameter and 30 mm thickness, comprised of 12,162 particles. The disc was in contact with the lateral walls in the X direction, whereas both the walls in the Y and Z directions were moved apart by a distance of 0.05 × height of initial rectangular assembly and 0.05 × diameter of the disc. During the test, the Y and Z walls had zero velocity whereas the X-lateral walls were moving towards each other using the same platen-loading logic described in the Uniaxial test Fig. 5.

During the test, the force (F) acting on the sample initiating by the movement of the X-lateral walls was

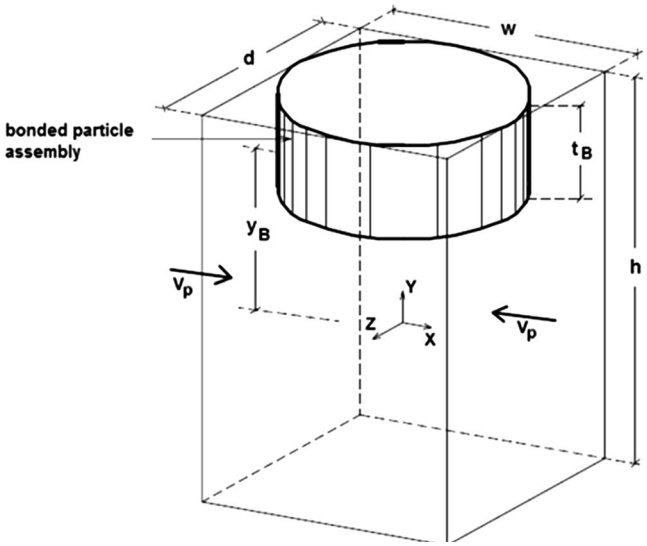

Fig. 5 Schematic of the PFC Brazilian disc (Itasca-Consulting-Group 2008c)

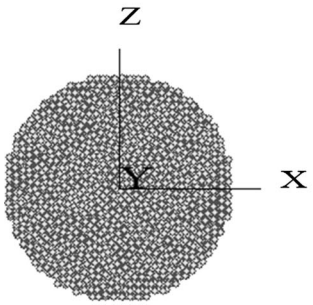

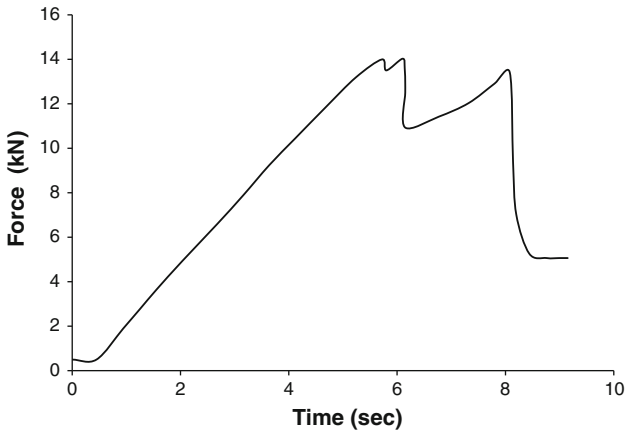

Fig. 6 Force acting on the platens of the Brazilian disc versus time. The sample fails under 14 kN

calculated and the maximum value was recorded reaching a maximum value and then decreasing as the sample failed. The same termination criterion, as in the Uniaxial test, was used therefore the test was terminated when the current average force became smaller than 0.01 times the previously recorded maximum force $(F < \alpha \times F_{\max})$. Figure 6 demonstrates the behaviour of the material until it reaches the ductile area and the point of its peak force 14KN. When a cylindrical sample is subjected in a compressive loading perpendicular to its axis and in a diametrical plane, it fails under tension (Wright 1955). The Brazilian tensile strength (6 MPa) is calculated by

$$\sigma_t = \frac{F_{\max}}{\pi R t_B}, \quad (1)$$

where $F_{\max}$ is the peak force acting on the platens and R and t_B are the radius and the thickness of the virtual disc, respectively.

This validates the values obtained from the literature and the fact that rocks are extremely weak in tension putting their tensile strength in the range of order of one-sixth to one-tenth of the UCS strength.

Simulation of hollow cylinder test

Even though hollow cylinder tests are commonly used in studies pertaining to wellbore instability and sand production, nonetheless, they are also used to investigate fracturing processes (Ewy et al. 1988; Elkadi and van Mier 2004; Enever and Bailin 2001; Ayob et al. 2009). As the mode of fluid application is a major determinant of the rock material behaviour, the simulated hollow cylinder test replicates the laboratory fracture test exploring the stress regime and the propagation of cracks. The virtual model was cylindrical with dimensions of diameter 37.8 mm, length 50 mm and comprised 12,840 particles of uniform size (Fig. 7). It is important to point out that although a PFC model in general demonstrates similar behaviour with that of a real rock, we do not correlate a PFC particle with a real rock grain. The virtual sample itself is a precise micro-structural assembly in its own right and should not be associated with the micro-structure of a rock (Itasca-Consulting-Group 2008c). The model has a hollow central region (pipe-like) with a diameter of 21.3 mm, along the axis of the cylinder following the layout of the laboratory sample.

During the laboratory experiment, the rock sample was placed inside a tube through which water was injected. The movement of the fluid through the body of the sample was activated by setting a pressure difference between the outer perimeter of the sample and its internal hollow core. The purpose of the hollow core was to allow the fluid's movement through the pipe to make the rock fully

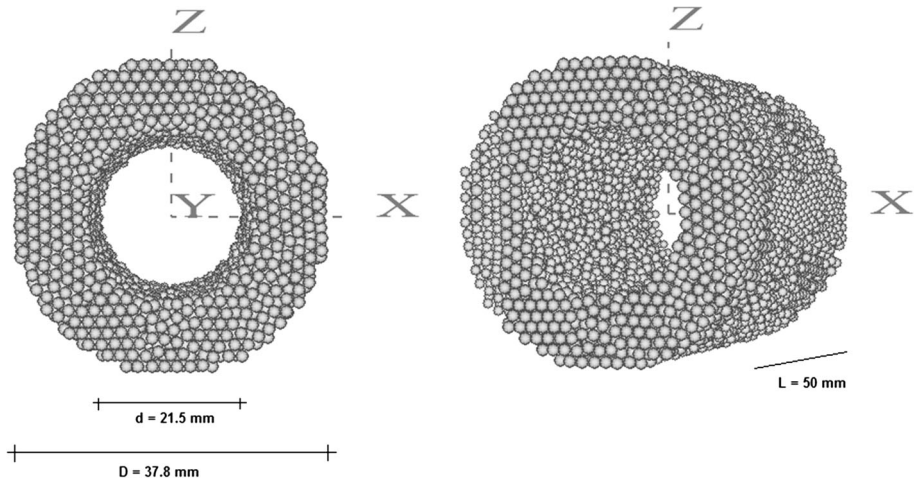

Fig. 7 Schematic of the virtual limestone model with a hollow cylindrical core

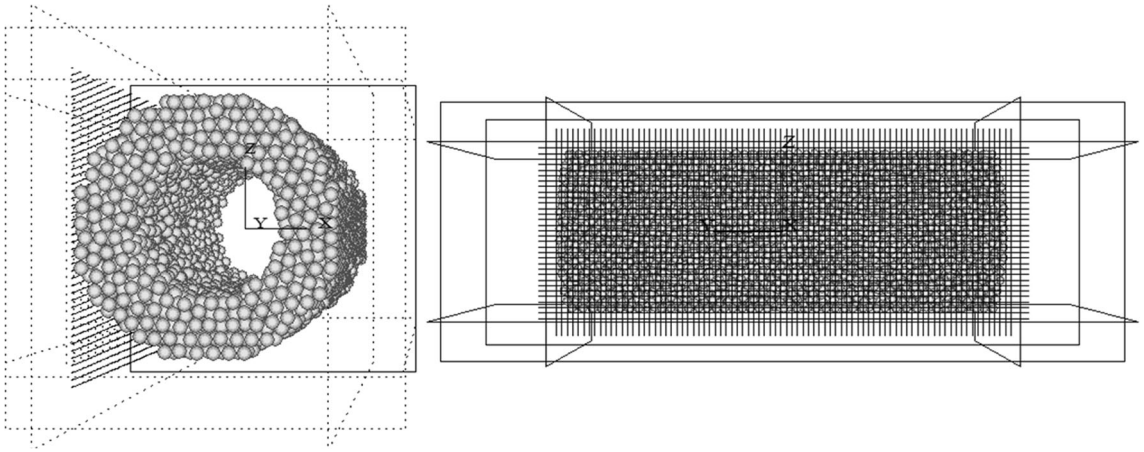

Fig. 8 The 3D mesh (filter) used to support the sample. Each side of the mesh consists of horizontal and vertical 1D walls

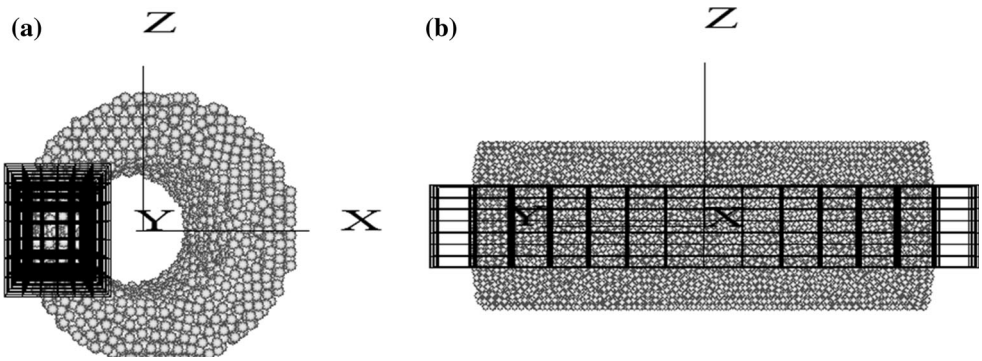

Fig. 9 Application of the fluid cell grid around a slice of the sample, **a** *front view*, and **b** *side view*

saturated keeping its internal pressure close to zero, while the external pressure was gradually increased. This pressure difference forced the fluid to radially penetrate the rock's body towards its core.

The fluid-flow logic was used for this work as a function already developed by the Itasca Company (Itasca-Consulting-Group 2008a). It can be considered as a two way couple as the fluid injection has altered the structure of the rock (in terms of fractures) and the fracturing also altered the path of the fluid flow. As the problem simulated in this paper is not diluted particle flow in a fluid, but instead, it is a densely pack medium with flow pass through it pores, the particle fluid rate has no significant impact on the model.

Initially, a three-dimensional mesh (filter) which encapsulated the sample was created, thus allowing the discharge of water through it. The mesh that consists of

one-dimensional (line) walls specified at regular locations around the sample has minor effect in terms of interaction with the particles. The purpose of the filter walls is mainly to provide basic support to the movement of the particle. The spacing between the line walls was set to be equal to the minimum ball radius of the sample. It is important that the filter is sufficiently dense to merely support the sample during the fluid flow, but not so dense as to interfere with the model's overall behaviour. Next, the fluid pressure boundary conditions had to be set. Due to software restrictions in terms of boundary conditions, a simplified but equivalent representation of the laboratory conditions had to be developed. More specifically, there is no way of defining a pressure boundary condition upon the fluid cells that do not reside at the edges of the fluid cell mesh therefore another equivalent concept had to be devised. An alternative approach to overcome this limitation in the PFC software was to use a rectangular slice of the assembly, instead of the whole cylindrical sample, applying the filter walls. The filer spacing was set equal to the particle radius of 1.0 mm in every direction (Fig. 8).

Moreover, a fluid cell grid was also applied to the rectangular slice of the assembly covering the outer perimeter and the inner hollow core of the model, as illustrated in Fig. 9. The whole assembly may be considered to consist of eight (8) of these slices. Since the actual laboratory experiment had radial symmetry (water flowing from the outside towards the inside in all directions along the z–x plane), it is valid to state that the flow through each slice should correspond to approximately 1/8th of the total flow through the complete assembly. The parameters defining the grid were its dimensions and the number of cells along each direction. There are no guidelines of the grid's parameters other than in case of a porous medium the cells should have a size comparable to that of a few particles. This is due to the fact that porosity and permeability are calculated through each cell, thus the cell grid must be coarse. During this test, 240 fluid cells were created, each with a cell size of $2.6 \times 8.3 \times 1.26$ mm. In the laboratory experiment, the sample was placed inside a tube where the fluid pressure was applied uniformly around the outer surface of the body of the rock. Therefore, the exerted forces at each point of the rock's outer surface was neutralised by an equal and opposite force on the other side of the sample which kept the sample in a static equilibrium position during the experiment. To model this effect, solid boundary walls were placed around the sample, except for the one on the left-hand side where the fluid was injected. The fixed impenetrable walls prevented the movement of the sample and emulated the sample equilibrium maintained during the laboratory experiment.

The pressure differential applied during the laboratory experiment was gradually increased starting from 8 MPa with a loading rate of 0.004 MPa/s until the failure of the sample in a time frame of about 8,400 s. To replicate the laboratory pressure inside the simulated test, the plot of the fluid pressure versus time, was divided into two regions, covering the periods of time 0–2,000 s, and 2,000–8,400 s, as shown in Fig. 10 (dashed). In the first region, the simulated fluid pressure was set to 8 MPa, which is the average of the plot points in that section (Fig. 10 solid black). In the second region of the plot, the pressure was gradually increased from 8 MPa until failure.

The small timestep inherent in the PFC simulations to ensure stability (typically of the order of tens of microseconds) resulted in impractical computational run-times when attempting to model the complete 8,400 s experiment. To alleviate this, the simulated time of the test had to be scaled down to a feasible value. The overall runtime of the shortened test was around 125 s, with the stable pressure region spanning for 31 s (=1/4 of total runtime) which corresponds to the 2,000 s region of the physical laboratory experiment (=1/4 of the total 8,362 s runtime). Due to the fact that the overall time of the test had to be scaled down the loading rate had to be scaled up for the physical and simulated tests to be equivalent, thus the pressure gradient was set to 0.12 MPa/sec. Even though in reality the increase of the pressure gradient will have an effect on the overall strength of the rock, in the case of the PFC assembly, the Navier–Stokes equation for incompressible fluid flow is pressure-free since there is no explicit mechanism for advancing the pressure in time. Furthermore the pressure gradient is not included in the formula thus does not affect the behaviour of the virtual assembly. Numerical tests had been carried out to confirm that this increase of loading rate has very little influence on the material behaviour of the sample.

To maintain the equilibrium of the sample, the pressure increment was performed in distinct steps which allowed the sample to reach a steady state with the current pressure step before moving to the next pressure step. To estimate an appropriate duration for each pressure step, the model was simulated several times under different pressures within the range of 8–33 MPa until it reached equilibrium in terms of the flow rate. Figure 11a illustrates the flow rate for constant pressure differentials of 13 and 30 MPa. It can be observed that the water discharge is stable within approximately 10 s. Thus, 10 s was deemed to be a suitable time period for the sample to adjust to the applied pressure step and ensure that although there is an overall pressure built-up during the experiment, the sample retains its equilibrium satisfying the criteria for steady and uniform flow. Figure 11b illustrates the applied fluid pressure for the simulated test, which remains stable for the first 25 s and then the applied pressure is increased by 1.2 MPa every 10 s.

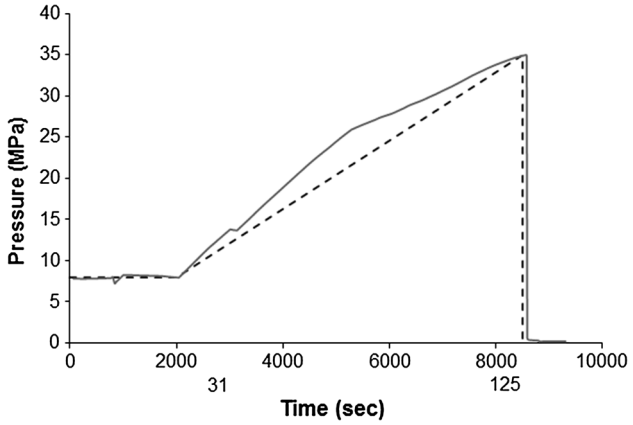

Fig. 10 Laboratory (*solid*) and simulated (*dashed*) fluid pressure differential applied on the outer surface of the sample as a function of time

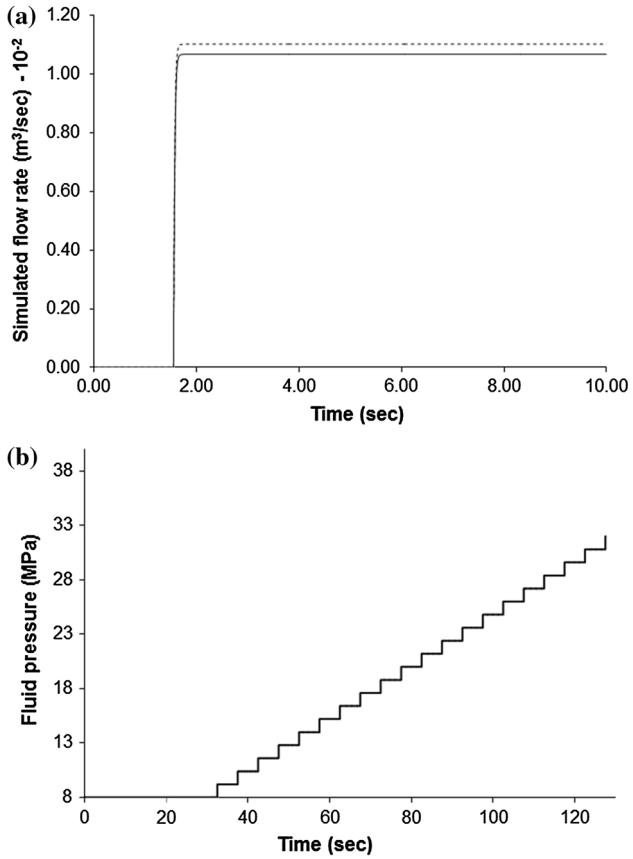

Fig. 11 **a** Simulated flow rate versus time for 13 MPa (*solid black*) and 30 MPa (*dashed*) constant pressure differential between the outer and inner perimeters of the limestone assembly, and **b** applied fluid pressure versus time during the simulation of the single phase flow through the limestone sample. The pressure is kept at 8 MPa for 25 s before starting to rise in steps of 1.2 MPa every 10 s. Sample failure occurs at 32.5 MPa

The simulated fluid was water with a density and viscosity of 1,000 kg/m^3 and 10^{-3} Pa.s, respectively. The described pressure gradient was applied to the outer side of the fluid cell grid (leftmost side as seen in Fig. 12) whereas the pressure on the inner side of the grid (rightmost side as seen in Fig. 12) was set to 0. Finally, to replicate the actual laboratory experiment in PFC the assumption that the fluid travels along the X axis had to be made.

Analytical/numerical solutions to the hollow cylinder test

Stress distribution

The aim of the hollow cylinder test was to replicate the laboratory loading conditions on a cylindrical limestone sample with a hollow core. The test provides an indication of the stress field of the PFC model and the overall behaviour of the assembly under high pressure differential. The equations are known as Lame's equations (University-of-Washington; Perry and Aboudi 2003; Ayobet al. 2009) and they are used to determine the stresses in thick-walled cylindrical pressure vessels (Fig. 13).

These are given by the following equations:

$$\sigma_r = A - \frac{B}{r^2} \tag{2}$$

$$\sigma_\theta = A + \frac{B}{r^2}, \tag{3}$$

where σ_r and σ_θ are the radial and tangential stresses, respectively, while A and B are constants given by:

$$A = \frac{P_i r_i^2 - P_0 r_0^2}{r_0^2 - r_i^2} \tag{4}$$

$$B = \frac{(P_i - P_0) r_i^2 r_0^2}{r_0^2 - r_i^2}. \tag{5}$$

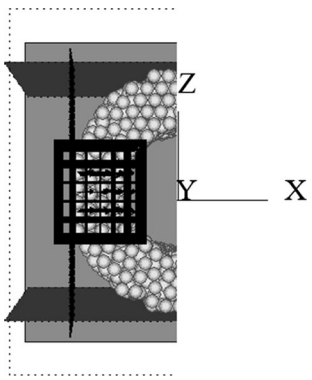

Fig. 12 Fluid pressure boundary conditions for the PFC model under the assumption that the movement of the fluid is horizontal. The pressure on the outer perimeter of the model in constantly increased, whereas the pressure inside the cavity is zero

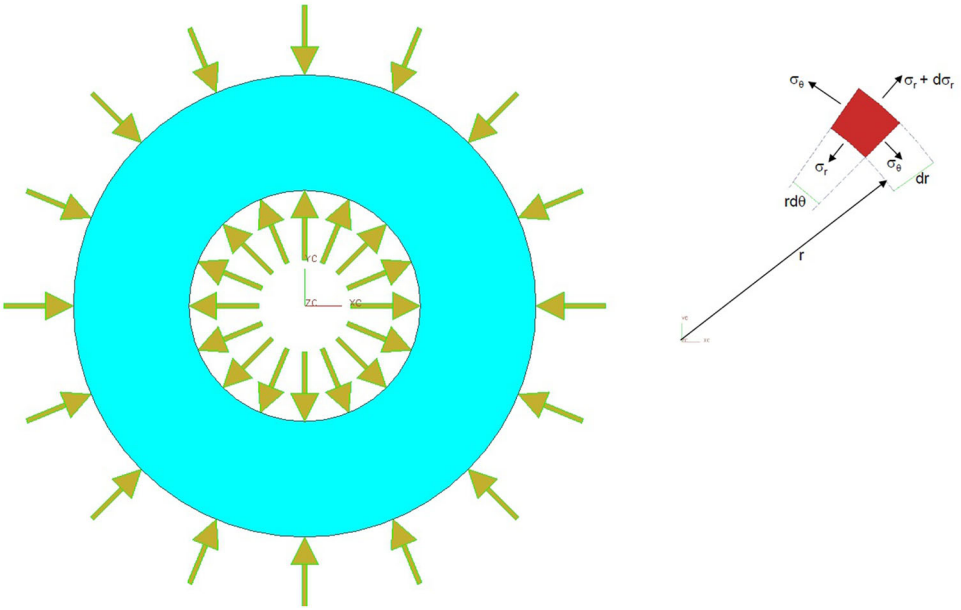

Fig. 13 Two-dimensional schematic of a hollow cylinder and an element at radius r from the centre of the cylinder (University-of-Washington)

Substituting Eqs. (4), (5) into (2) and (3) we conclude

$$\sigma_\theta = \frac{P_i r_i^2 - P_0 r_0^2}{r_0^2 - r_i^2} + \frac{(P_i - P_0) r_i^2 r_0^2}{\left(r_0^2 - r_i^2\right) r^2} \tag{6}$$

$$\sigma_r = \frac{P_i r_i^2 - P_0 r_0^2}{r_0^2 - r_i^2} - \frac{(P_i - P_0) r_i^2 r_0^2}{\left(r_0^2 - r_i^2\right) r^2}. \tag{7}$$

For the longitudinal stress acting on the cut of the cylinder, force equilibrium law is used where a pressure P_i acts on an area πr_i^2 and a pressure P_0 acts on an area πr_0^2, thus the overall stress acts on the area $\pi\left(r_0^2 - r_i^2\right)$ and is given by:

$$\sigma_L = \frac{P_i r_i^2 - P_0 r_0^2}{r_0^2 - r_i^2}. \tag{8}$$

For the case of a closed ends cylinder with zero internal pressure P_i and r_i internal radius, P_0 external pressure and r_0 external radius, the stresses at a given distance r are given by:

$$\sigma_\theta = \frac{-P_0 r_0^2}{r_0^2 - r_i^2}\left[1 + \frac{r_i^2}{r^2}\right],\ \sigma_r = \frac{-P_0 r_0^2}{r_0^2 - r_i^2}\left[1 - \frac{r_i^2}{r^2}\right],$$
$$\sigma_L = \frac{-P_0 r_0^2}{r_0^2 - r_i^2} \tag{9}$$

where σ_θ, σ_r and σ_L are the tangential, radial and longitudinal, respectively.

Fluid flow

The aim of the fluid flow test in three dimensions is to replicate the laboratory hydraulic fracturing test of the cylindrical limestone sample. The test gives a good indication of the material's hydraulic conductivity and the behaviour of the sample under high pressure. The flow rate, in m^3/sec, for the liquid flow through the porous media is given by

$$Q = qA \tag{10}$$

where A is the cross-sectional area perpendicular to the direction of flow, and q is the velocity of the liquid given by Darcy's Law (Dullien 1979; Nield and Bejan 2006):

$$q = -\frac{k}{\mu}(\nabla P - \rho g \nabla z), \tag{11}$$

where k is the absolute permeability of the sample, μ is the fluid's dynamic viscosity, P is the fluid pressure, g is the magnitude of the gravitational acceleration, ρ is the density of the fluid, z is the elevation in the direction of the flow (which in this case is set to zero as the fluid moves horizontally).

In steady state, the velocity q in Eq. (11) becomes the interstitial velocity u_0 of the fluid. This can be derived from the combination of the well-known Navier–Stokes and Erqun's relations, Eqs. (12) and (13), respectively, for fluid flow through packed bed which for the case of a fixed homogeneous porous material takes the form (Itasca-Consulting-Group 2008a) (University-of-Washington; Jia et al. 2009):

$$\rho \frac{\partial \varepsilon \vec{u}}{\partial t} + \rho \overrightarrow{u_0} \cdot \nabla(\varepsilon \vec{u}) = -\int \nabla p + \mu \nabla^2 (\varepsilon \vec{u}) + f_{\vec{\beta}} \tag{12}$$

$$\frac{\Delta_p}{L} = \frac{150\mu(1-\varepsilon)^2 u_0}{\varepsilon^3 \overline{d_p}^2} + \frac{1.75(1-\varepsilon)\rho u_0^2}{\varepsilon^3 \overline{d_p}}, \tag{13}$$

where, μ is the viscosity of the fluid, ε is the porosity, $f_{\vec{\beta}}$ is the body force per unit volume, the interstitial fluid velocity is denoted as u_0 L is the height of the bed, Δ_p is the pressure difference, $\overline{d_p}$ is the mean particle diameter, and 150 and 1.75 are constants obtained by experimentation.

As already mentioned in the Uniaxial test, during the typical generation process the sample is packed with particles of uniform size. At this stage the assembly is reaching equilibrium with the use of some stabilizing strategies (i.e. target isotropic stress) thus all body forces acting on the particles prior to fluid movement are being eliminated. In the fluid scheme of PFC3D, driving forces from fluid flow are applied to particles as body forces, making the body force of Eq. (12) the only one acting. Furthermore, local non-viscous damping is provided by PFC3D meaning that body forces approach zero for steady motion. If we assume that the assembly of particles is similar to a packed bed, then when there is no flow through the packed bed the net gravitational force (including buoyancy) acts downward. When the flow starts moving upward, friction forces act upward and counterbalance the net gravitational force. For high enough fluid velocities, the friction force is large enough to lift the particles (University-of-Washington; Itasca-Consulting-Group 2008a).

Generally, two different formulations can be encountered for the fluid velocity in porous flow: one is the aforementioned interstitial velocity u_0, and the other is the macroscopic or Darcy velocity $\varepsilon\vec{u}$. The interstitial velocity is the actual velocity of a fluid parcel flowing through the pore space. The macroscopic velocity is the volumetric flow rate per unit cross-sectional area. This is a non-physical quantity calculated on the basis that the flow occurs across the entire cross-sectional area, although in reality the flow only occurs in between the pore space.

In the case of steady uniform flow, the macroscopic velocity is assumed to be constant and thus the terms on the left-hand side of Eq. (12) become zero. On the right-hand side, the term $-\in \nabla \mathrm{p}$ is the applied pressure gradient, $\mu\nabla^2(\varepsilon\vec{v})$ denotes the momentum loss due to viscosity, and $f_{\vec{\beta}}$ corresponds to the drag force exerted by the particles on the fluid. The viscous term $\mu\nabla^2(\varepsilon\vec{v})$ can be assumed to be negligible in comparison to the other two terms.

Combining Eqs. (11) and (12) the second-order Eq. (13) gives a solution of

$$u_0 = \frac{\sqrt{(1-\varepsilon)4\overline{d_\mathrm{p}}^3\varepsilon^3 \cdot_\mathrm{p} \rho 150 + (\varepsilon-1)^4\mu^2 150^2} - 150\mu(\varepsilon-1)^2}{2\overline{d_\mathrm{p}}(1-\varepsilon)\rho 1.75}. \quad (14)$$

Equation (15) was used during the simulations to provide the volumetric flow rate results of the discharging liquid through the virtual assembly.

$$q_{\mathrm{vol}} = u_0 \times A \quad (15)$$

where A is the simulated cross-sectional area of the slice perpendicular to the direction of flow.

As already discussed, the macroscopic properties of a real rock cannot be directly described in a DEM model due to the fact that the particle size distribution of the virtual model does not have to copy the actual rock's grain size distribution. This results to a mismatch between the hydraulics of the real rock and the virtual model in terms of pressure drop and fluid relative velocity. Furthermore, it is actually advantageous to decouple the micro-properties of the DEM specimen from those of the actual rock. This is because attempts to match the porosity of the actual rock would lead to a broader particle size distribution, which in turn lowers the timestep resulting to impractical simulation time. For these reasons, it was considered best to use calibration factors that will alter the fluid flow parameters of the virtual model.

According to Ergun's relation in Eq. (13)

$$\frac{\Delta_\mathrm{p}}{L} = C_1\mu u_0 + C_2\rho u_0^2, \quad (16)$$

where

$$C_1 = \frac{150(1-\varepsilon)^2}{\varepsilon^3\overline{d_\mathrm{p}}^2}$$

$$C_2 = \frac{1.75(1-\varepsilon)}{\varepsilon^3\overline{d_\mathrm{p}}} \quad (17)$$

To match the pressure drop of the DEM specimen with that of an actual rock the terms of Eq. (14) on the right-hand side should be scaled. The following process results to the scaling factors of viscosity and density used in the virtual model.

Combining C_1 from Eq. (16) with the Kozeny–Carman equation regarding the permeability of a real rock given by

$$k = \frac{1}{180}\frac{\varepsilon^3 d^2}{(1-\varepsilon)^2} \quad (18)$$

It is concluded that C_1 corresponds to the inverse of permeability for the DEM specimen and it is given as follows

$$C_1 = \frac{150(1-\varepsilon)^2}{\varepsilon^3\overline{d_\mathrm{p}}^2} = \frac{150}{180}\frac{1}{k} \quad (19)$$

It is clear that the permeability depends on the specimen's micro-parameters thus a calibration factor a_μ was multiplied with the above equation to match the specimen's parameters with the actual's rock with the use of the following relation

$$[C_1]_{\mathrm{PFC}} \times a_\mu = \left[\frac{150}{180}\frac{1}{k}\right]_R, \quad (20)$$

where the terms PFC and R mean that the equations inside the brackets refer to the PFC model and the real rock,

respectively. According to the literature, the permeability for a limestone rock lies within the range of 2×10^{-11}–4.5×10^{-10} cm^2 (Nield and Bejan 2006). Choosing a mean value for permeability, the calibration factor is calculated as follows and it refers to the viscosity term of Eq. (16)

$$a_\mu = \left[\frac{\varepsilon^3 \overline{d_p}^2}{150(1-\varepsilon)^2}\right]_{PFC} \frac{150}{180}\frac{1}{k}. \quad (21)$$

The same process was followed regarding the calibration factor a_ρ referring to the density parameter of Eq. (16) with the use of the following relation

$$[C_2]_{PFC} \times a_\rho = \left[\frac{1.75(1-\varepsilon)}{\varepsilon^3 d}\right]_R. \quad (22)$$

Using Kozeny–Carman Eq. (17) to calculate the diameter d of the real rock and install it into Eq. (21), the calibration factor for density is given by

$$a_\rho = \frac{\left[\varepsilon^3 \overline{d_p}^2\right]_{PFC}}{\left[\varepsilon^{3/2}\sqrt{180k}\right]_R}. \quad (23)$$

In terms of coding these factors are used by multiplying the viscosity term with a_μ and the density term with a_ρ.

Results and discussions

Figure 14 illustrates the results of the stress distribution in the centre of the slice under the applied fluid pressure differential, whereas Fig. 15 demonstrates the stress distribution based on the analytical solution (Lame's equations). Both the tangential and radial stresses change linearly with the applied fluid pressure bringing the analytical and numerical results in good qualitative agreement. This also validates the fact that the bonded-assembly (DEM) approach, followed by the PFC software, is specifically designed to reproduce stresses–strains in microscopic media and that Lame's theory can be adequately applied. Quantitatively, the difference in the magnitude of stresses can be attributed to the fact that Lame's equations assume a continuous medium whereas the virtual model is non-continuous.

A micro-crack in the PFC3D sample is the subsequent bond breakage between two bonded particles. Thus the number and position of possible micro-cracks are limited by the number and position of the parallel bonds in the virtual sample. The shape of each micro-crack is cylindrical whose axis is located alongside the line connecting the two neighbourhood particles. The parameters that define each micro-crack are its thickness (t_c), radius (R_c) and centroid location. The thickness is the distance

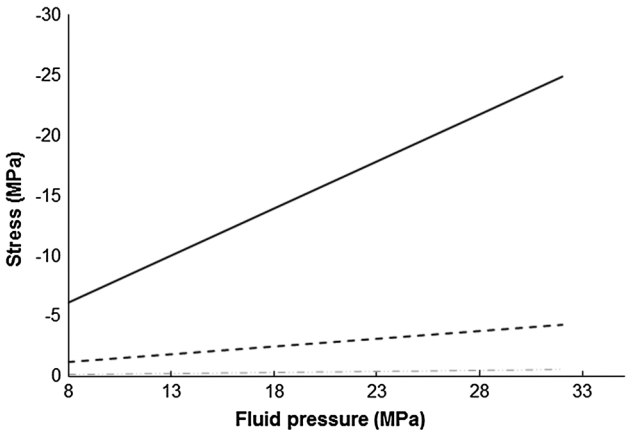

Fig. 14 Simulated stress field at the middle of the slice [radial (σ_{xx}) *dashed grey*, longitudinal (σ_{yy}) *dashed black*, tangential (σ_{zz}) *solid black*] versus fluid pressure differential

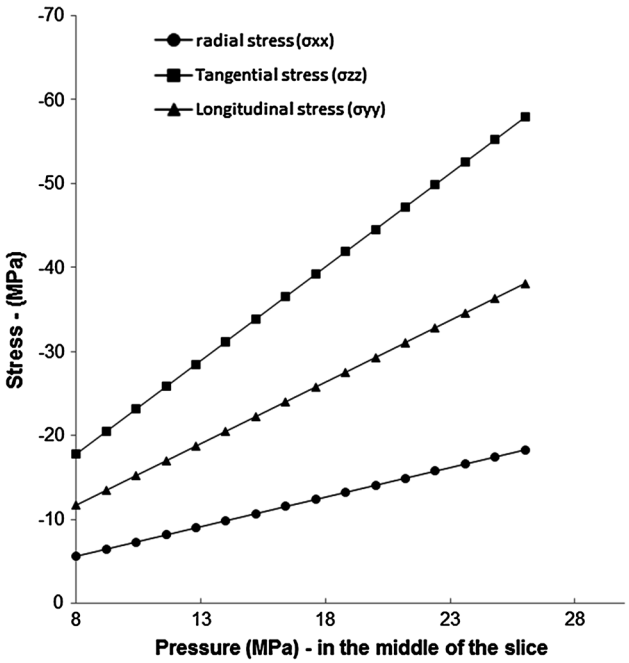

Fig. 15 Stress field versus fluid pressure differential at the middle of the slice according to Lame's equations [radial (σ_{xx}) *circle*, longitudinal (σ_{yy}) *triangle*, tangential (σ_{zz}) *square*)

between the two neighbourhood particles, the radius is the intersection between the cylinder's bisection plane and a stretched membrane among two neighbourhood particles and the centroid is the centre of the bond and is located in the middle of the line formed by the centres of the two neighbourhood particles (Fig. 16). Figures 17 and 18 demonstrate the fracturing process of the virtual assembly at different stages under the gradual increase of the fluid pressure differential resulting to its total collapse, and the development of the micro-cracks versus the applied fluid pressure.

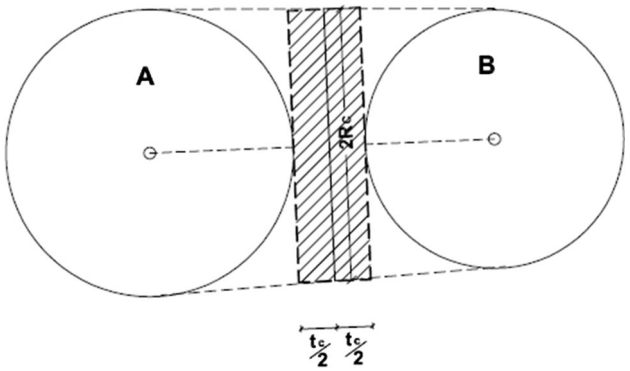

Fig. 16 Schematic of the geometry and location of each micro-crack (Itasca-Consulting-Group 2008b)

A micro-crack can occur either in the perpendicular (normal) or shear direction with respect to the bond plane. It was found that there were 5,000 micro-cracks formed inside the rectangular slice with 3,512 of them in the normal direction and 1,493 in the shear direction.

It can be observed that even though failure forms early at the outside perimeter of the sample, it propagates in a lower rate compared to the crack propagation of the inner surface. The latter begins from the vicinity of the inner surface at roughly 26 MPa and expands outwards as a result of the stress distribution, leading to sample failure at 32.3 MPa where the particles are thrown inside the cavity. This is in very good agreement with the failure point of about 35 MPa measured during the laboratory experiment and close to the material's UCS strength measured by the Uniaxial test. The fracturing pattern is dominated by shear and compressive stresses forming a total of 5,000 micro-cracks at the failure point.

The failure mode also comes in agreement with Lame's theory indicating that all the principal stresses are compressive and even though the highest radial compressive stress occurs at the outer surface, which is the same as the applied fluid pressure, the maximum compressive stresses are tangential, and act in the vicinity of the inner diameter [Eq. (6)]. Thus, relatively, compressive stresses are high towards the inner surface. The longitudinal stress remains constant acting in the axial direction and the shear stress is maximum at the inner surface. The theoretical explanation of this is shown in Fig. 19.

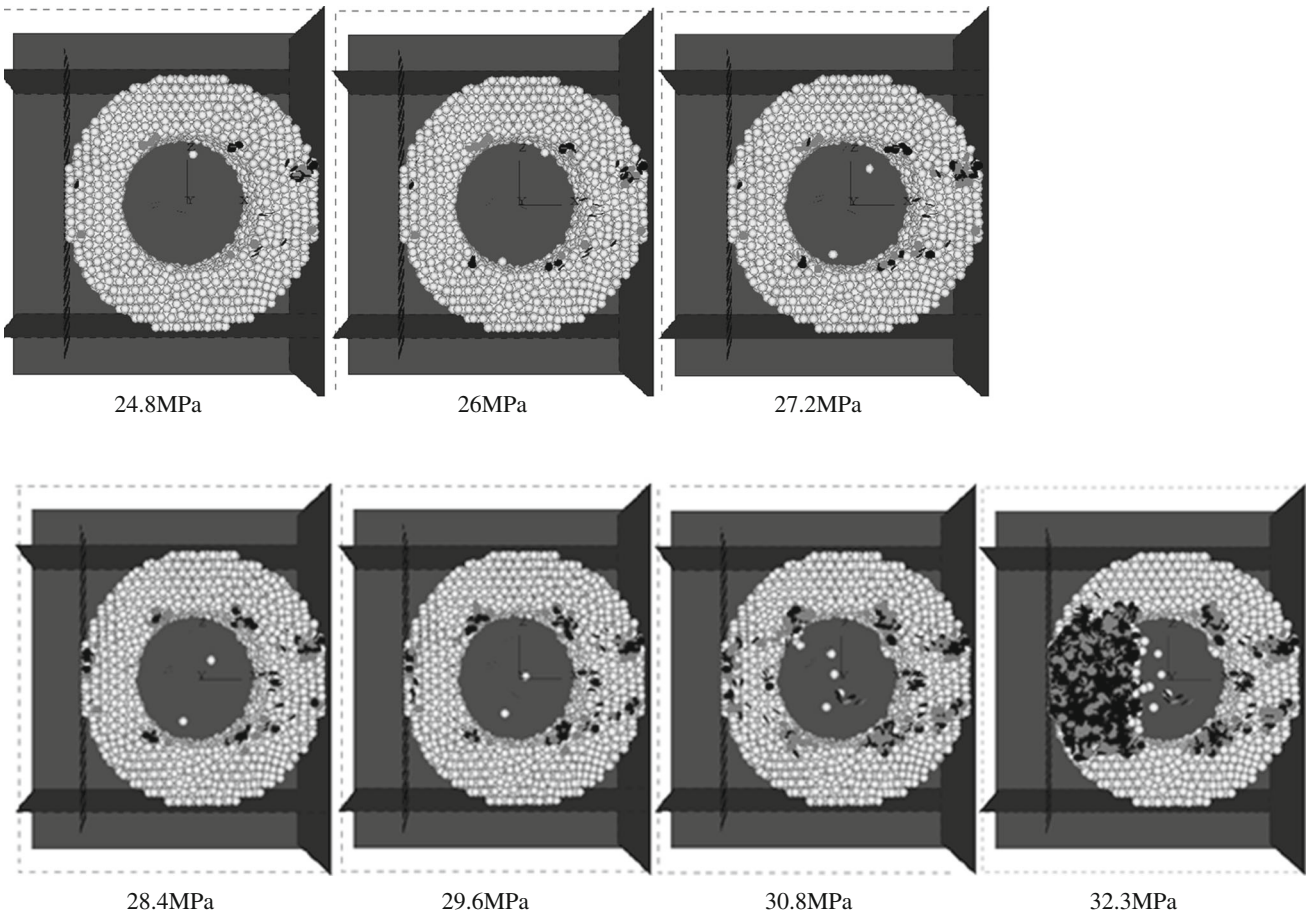

Fig. 17 Initiation and propagation of micro-cracks of the virtual assembly at different stages

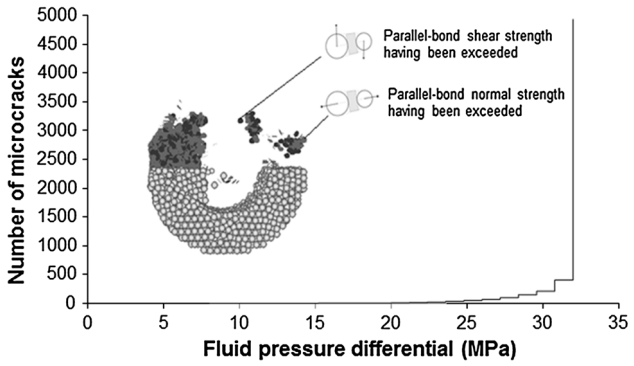

Fig. 18 Total number of micro-cracks versus the applied fluid pressure differential (the *black dots* indicate the parallel-bond breakage in the shear direction, whereas the *grey dots* indicate the parallel-bond breakage in the normal direction)

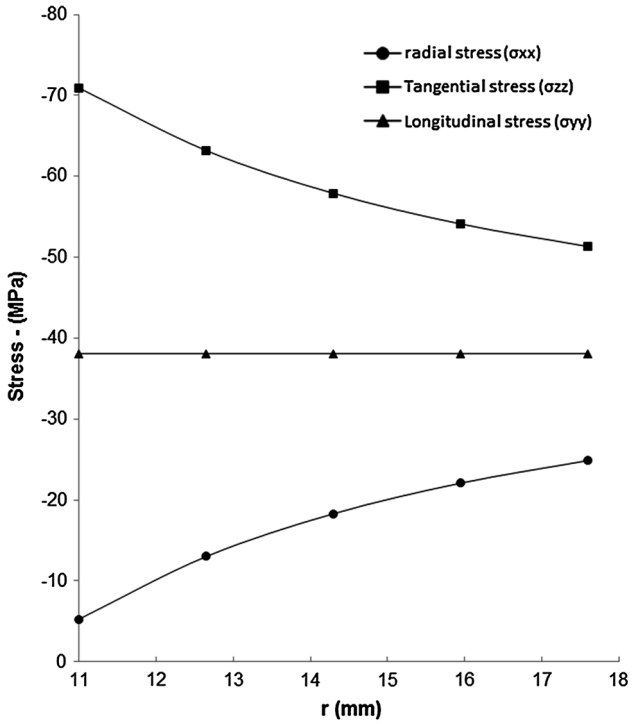

Fig. 19 Variation of the stress field along the wall thickness according to Lame's equations [radial (σ_{xx}) *circle*, longitudinal (σ_{yy}) *triangle*, tangential (σ_{zz}) *square*)

Figure 20 demonstrates the resulting flow rates of water, from all calculations methods, through the slice during the simulated test. According to the graph, as soon as the fluid starts to penetrate the sample a small flow rate is recorded which remains stable during the steady pressure regime (0–25 s). As the pressure gradient is varied (25–125 s), the simulated flow rate increases gradually reaching 0.035 m^3/s after 125 s. It can be observed that for the steady pressure regime both the simulated flow rate and the analytical flow rates (Darcy and steady-state solution) are in very good agreement.

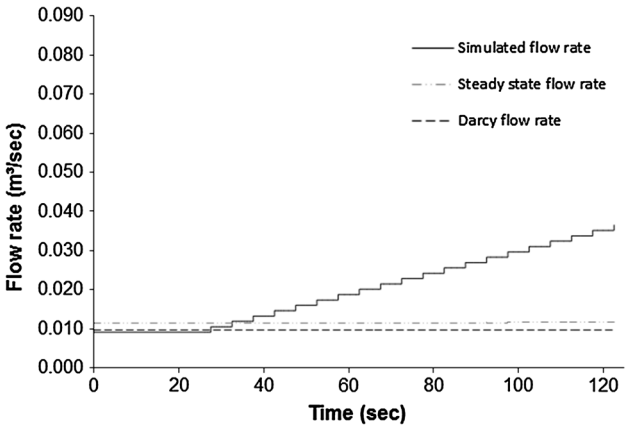

Fig. 20 Simulated flow rate of water through the slice versus time

Table 4 Summary of the hydraulic fracturing simulation

Fluid flow results for the first 25 s	
Number of cracks	5,000 (3,512 normal, 1,493 shear)
Permeability (m^2)	6.68×10^{-9}
Darcy flow rate (m^3/s)	0.096×10^{-2}
Steady-state flow rate (m^3/s)	0.0115×10^{-2}
Simulated flow rate (m^3/s)	0.091×10^{-2}

Table 4 summarises the results from the fluid flow fracturing test during the steady pressure regime on the rectangular limestone slice. It is clear that all three different flow rates are in very good agreement for the steady pressure regime. According to results, the simulated flow rate is closer to Darcy's flow rate than to steady-state one. This can be attributed to the fact that the steady-state solution is referred to an idealised flow assuming that the pressure gradient and particle drag forces due to fluid flow are much greater than viscous losses. This is due to assumptions made that relate the viscous loses to the macroscopic fluid velocity. The steady-state solution assumes uniformity in the velocity gradient resulting in an underestimation of the losses due to viscous stresses. However, the numbers indicate that the disparity between the steady-state flow and the simulated flow is negligible.

Conclusions

This paper presents the computational modelling of the hydraulic fracturing test for a limestone sample, and includes a series of Uniaxial and Brazilian tests with the use of the DEM approach. The purpose of this work was to calibrate the microscopic material parameters and to use the laboratory test results to validate the developed DEM model. Model calibration was followed by the simulation

of the hollow cylinder fracturing test with model configurations identical or close to the conditions of the laboratory test. The mechanical response of the rock specimen to the fluid injection was analysed by evaluating the volumetric flow rate at which the fluid was discharged, the initiation and propagation of cracks through the simulated model and the relation between its UCS strength and the failure pressure.

In PFC, a generalised form of Navier–Stokes equation that account for fluid–solid interaction is solved using a grid fluid flow scheme. We have adopted these formulations herein by firstly, incorporating this technique into the DEM simulation of a bonded particle assembly representing an intact material. Secondly, an extension of its applicability is demonstrated via the modelling of hollow cylinder laboratory test. Applications of this sort, where direct numerical and experimental comparisons were carried out, are still lacking.

Both the simulated model and the physical limestone proved to behave in a similar manner. The fluid flow results were found to be in very good agreement with the laboratory observations in terms of the fracture pattern and the geo-mechanical behaviour, showing that the sample fails under 32.3 MPa, very close to the failure point measured during the laboratory test and close to the UCS strength of the sample.

A series of similar tests on samples of different strengths were also performed, which is not presented for the sake of brevity. All the tests showed a similar behaviour. The maximum fluid pressure load for samples of high strength was almost identical to their UCS strength, while failure followed the same general pattern. The combination of all the results for samples of low and high strength, aims to provide a valuable outcome for EOR and/or EGR applications since it can contribute a further insight towards estimations of safe injection pressures in cases of reservoirs with known strength. The investigation of the fracturing process can also be useful not only to prevent failures that may lead to leakages but also to control fractures towards safer reservoir productivity.

Acknowledgments The authors would like to thank the School of Civil Engineering and the Energy Technology and Innovation Initiative (ETII) of the School of Process, Environmental and Materials Engineering, University of Leeds for sponsoring this research. The authors also appreciate the provision of experimental facilities by the Wolfson Multiphase Flow Laboratory of the School of Earth and Environment, University of Leeds.

References

Akram MS, Sharrock GB (2009) Physical and Numerical Investigation of a Cemented Granular Assembly under Uniaxial and Triaxial Compression. Paper presented at the 43rd US Rock Mechanics Symposium and 4th US-Canada Rock Mechanics Symposium, Asheville

Aminuddin NJPNIM (2011) Scatter-plot analysis of microcracks pattern behaviour of Weathered Limestone at Batu Caves, Malaysia. EJGE 16:1639–1650

Ayob AB, Tamin MN, Elbasheer MK (2009) Pressure limits of thick-walled cylinders. In: International MultiConference of Engineers and Computer Scientists 2009, Hong Kong, March 18–20

Bachu S, Bennion B (2008) Effects of in situ conditions on relative permeability characteristics of CO_2-brine systems. Environ Geol 54(8):1707–1722. doi:10.1007/s00254-007-0946-9

Blunt M, Fayers FJ, Orr FM Jr (1993) Carbon dioxide in enhanced oil recovery. Energy Convers Manag 34(9–11):1197–1204. doi:10.1016/0196-8904(93)90069-m

Bouteca MJS, JP, Vincke O (2000) Constitutive law for permeability evolution of sandstones during depletion. Paper presented at the SPE International Symposium on Formation Damage Control, Louisiana

Boutt DF, Cook BK, McPherson BJOL, Williams JR (2007) Direct simulation of fluid-solid mechanics in porous media using the discrete element and lattice-Boltzmann methods. J Geophys Res Solid Earth 112(B10):B10209. doi:10.1029/2004JB003213

Bruno MS (1994) Micromechanics of stress-induced permeability anisotropy and damage in sedimentary rock. Mech Mater 18(1):31–48. doi:10.1016/0167-6636(94)90004-3

Bryant S, King P, Mellor D (1993) Network model evaluation of permeability and spatial correlation in a real random sphere packing. Transp Porous Med 11(1):53–70. doi:10.1007/bf00614635

Chang SC (1987) Micromechanical modelling of constitutive relations for granular materials. In: Jenkins JT, Satake M (eds) Micromechanics of granular materials. Elsevier, Amsterdam, pp 271–279

Chen S, Doolen GD (1998) Lattice Boltzmann method for fluid flows. Annu Rev Fluid Mech 30:329–364. doi:10.1146

Dong S (2007) Direct numerical simulation of turbulent Taylor–Couette flow. J Fluid Mech 587:373–393. doi:10.1017/S0022112007007367

Dullien FAL (1979) Porous media: fluid transport and pore structure, 2nd edn. Academic Press Inc, New York

Elkadi AS, van Mier JGM (2004) Scaled hollow-cylinder tests for studying size effect in fracture processes of concrete. In: Paper presented at the fracture mechanics of concrete structures, vol 1. USA, pp 229–236

Enever J, Bailin W (2001) Scale effects in hollow cylinder tests. In: Proceedings of the Asian Rock Mechanics Symposium; 209–212. A A Balkema, p 4

Eshiet KI, Sheng Y, Jianqiao Y (2013) Microscopic modelling of the hydraulic fracturing process. Environ Earth Sci 68(4):1169–1186. doi:10.1007/s12665-012-1818-5

Eslami JGD, Hoxha D (2010) Estimation of the damage of a porous limestone from continuous (P- and S-) wave velocity measurements under uniaxial loading and different hydrous conditions. Geophys J Int 183:1362–1375. doi:0.1111/j.1365-246X.2010.04801.x

Ewy RT, Cook GW, Myer LR (1988) Hollow cylinder tests for studying fracture around underground openings. Paper presented at the The 29th US Symposium on Rock Mechanics (USRMS), Minneapolis, MN, June 13–15

Ferfera FMR, Sarda JP, Boutéca M, Vincké O (1997) Experimental study of monophasic permeability changes under various stress paths. Int J Rock Mech Min Sci 34(3–4):126. doi:10.1016/S1365-1609(97)00105-6

Funatsu T, Ishikawa M, Shimizu N, Li Q, Seto M (2007) Study on the numerical modeling of crack propagation in rock by the distinct element method. Paper presented at the 11th Congress of the International Society for Rock Mechanics

Gil I, Roegiers JC, Hart R, Shimizu Y (2005) Modeling the Mechanical Properties of Antler Sandstone using a Discrete Element Model. Paper presented at the 40th Symposium on Rock Mechanics: Rock Mechanics for Energy, Mineral and Infrastructure Development in the Northern Regions, Anchorage, Alaska

Gordalla B, Ewers U, Frimmel F (2013) Hydraulic fracturing: a toxicological threat for groundwater and drinking-water? Environ Earth Sci 70(8):3875–3893. doi:10.1007/s12665-013-2672-9

Hallsworth CR, Knox RW O' B (1999) British Geological Survey: Classification of sediments and sedimentary rocks. vol 3. Nottingham

Hanson ME, Anderson GD, Shaffer RJ (1980) Theoretical and experimental research on hydraulic fracturing. J Energy Resour Technol Trans ASME 102(2):92–98

Holt RM (1990) Permeability reduction induced by a non-hydrostatic stress field. SPE Form Eval 5(4):444–448. doi:10.2118/19595-PA

IEAGHG (2011b) Caprock Systems for Geological Storage. vol 01

IPCC (2007a) Climate Change 2007: "Synthesis Report"

IPCC (2007b) Technical Summary. IPCC WG1 AR4 Report

Itasca-Consulting-Group (2008a) Particle flow code in 3 dimensions (PFC3D). ICG, Minneapolis

Itasca-Consulting-Group (2008b) User's Guide 1: Introduction. Minneapolis

Itasca-Consulting-Group (2008c) User's Guide 3: PFC FishTank. Minneapolis

Jaeger JC, Cook NGW, Zimmerman RW (2009) Fundamentals of rock mechanics. Wiley-Blackwell, New York

Jia Y, Li Y, Hlavka D (2009) Flow through packed beds. University-of-Rochester, New York

Jin H, Gao L, Sheng L, Porter R et al (2012) Opportunities for early Carbon Capture Utilisation and Storage development in China. 13:13

Kissinger A, Helmig R, Ebigbo A, Class H, Lange T, Sauter M, Heitfeld M, Klünker J, Jahnke W (2013) Hydraulic fracturing in unconventional gas reservoirs: risks in the geological system, part 2. Environ Earth Sci 70(8):3855–3873. doi:10.1007/s12665-013-2578-6

Knill JL, Cratchley CR, Early KR, Gallois RW, Humphreys JD, Newbery J, Price DG, Thurrell RG (1970) The logging of rock cores for engineering purposes. vol 3. Geological Society Engineering Group Working Party Report

Lange T, Sauter M, Heitfeld M, Schetelig K, Brosig K, Jahnke W, Kissinger A, Helmig R, Ebigbo A, Class H (2013) Hydraulic fracturing in unconventional gas reservoirs: risks in the geological system part 1. Environ Earth Sci 70(8):3839–3853. doi:10.1007/s12665-013-2803-3

Li L, Holt RM (2001) Simulation of flow in sandstone with fluid coupled particle model. Paper presented at the Rock Mechanics in the National Interest, Elsworth

Martinez D (2012) Fundamental hydraulic fracturing concepts for poorly consolidated formations. University of Oklahoma, Norman

Mikkelsen M, Jorgensen M, Krebs FC (2010) The teraton challenge. A review of fixation and transformation of carbon dioxide. Energy Environ Sci 3(1):43–81

Moin P, Mahesh K (1998) Direct numerical simulation: a tool in turbulence research. Annu Rev Fluid Mech 30:539–578

Nield AD, Bejan A (2006) Convection in Porous Media, vol 3. Springer, Berlin

Olsson O, Weichgrebe D, Rosenwinkel K-H (2013) Hydraulic fracturing wastewater in Germany: composition, treatment, concerns. Environ Earth Sci 70(8):3895–3906. doi:10.1007/s12665-013-2535-4

Parker ME, Meyer JP, Meadows SR (2009) Carbon dioxide enhanced oil recovery injection operations technologies (Poster Presentation). Energy Procedia 1(1):3141–3148. doi:10.1016/j.egypro.2009.02.096

Perry J, Aboudi J (2003) Elasto-plastic stresses in thick walled cylinders. J Press Vessel Technol 125(3):248–252. doi:10.1115/1.1593078

Potyondy DO, Cundall PA (2004) A bonded-particle model for rock. Rock Mech Min Sci 41:1329–1364. doi:10.1016

Riedl J, Rotter S, Faetsch S, Schmitt-Jansen M, Altenburger R (2013) Proposal for applying a component-based mixture approach for ecotoxicological assessment of fracturing fluids. Environ Earth Sci 70(8):3907–3920. doi:10.1007/s12665-013-2320-4

Tomiczek K (2003) Modeling of sandstone rock samples using PFC2D code. Paper presented at the Numerical Modeling in Micromechanics via Particle Methods, Lisse

Tsuji Y, Kawaguchi T, Tanaka T (1993) Discrete particle simulation of two-dimensional fluidized bed. Powder Technol 77(1):79–87. doi:10.1016/0032-5910(93)85010-7

University-of-Stanford Some Useful Numbers on the Engineering Properties of Materials. http://www.stanford.edu/~tyzhu/Documents/Some%20Useful%20Numbers.pdf. Accessed Sept 2013

University-of-Washington flow through packed beds. http://faculty.washington.edu/finlayso/Fluidized_Bed/FBR_Fluid_Mech/packed_beds_scroll.htm. Accessed Nov 2013

University-of-Washington Thick wall cylinders. http://courses.washington.edu/me354a/Thick%20Walled%20Cylinders.pdf. Accessed Nov 2013

Walton K (1987) The effective elastic moduli of a random packing of spheres. J Mech Phys Solids 35(2):213–226. doi:10.1016/0022-5096(87)90036-6

Wilkins SJ, Naruk SJ (2007) Quantitative analysis of slip-induced dilation with application to fault seal. AAPG Bull 91(1):97–113. doi:10.1306/08010605177

Wright PJF (1955) Comments on an indirect tensile test in concrete cylinders. Magazine of Concrete Research 7 (20):87–96

Xu BH, Yu AB (1997) Numerical simulation of the gas-solid flow in a fluidized bed by combining discrete particle method with computational fluid dynamics. Chem Eng Sci 52(16):2785–2809. doi:10.1016/S0009-2509(97)00081-X

Zhang X, Last N, Powrie W, Harkness R (1999) Numerical modelling of wellbore behaviour in fractured rock masses. J Pet Sci Eng 23(2):95–115. doi:10.1016/S0920-4105(99)00010-8

Ziqiong Z (1989) NGWC stress induced microcrack geometry at failure in unconfined and confined axial compressive tests. In: 30th US symposium on rock mechanics (USRMS), Morgantown, WV. American Rock Mechanics Association (ARMA)